Applied Catalysis B: Environmental 115–116 (2012) 117–128

Contents lists available at SciVerse ScienceDirect

Applied Catalysis B: Environmental

journal homepage: www.elsevier.com/locate/apcatb

Gold catalysts supported on nanostructured Ce–Al–O mixed oxides prepared by organic sol–gel

Elena Smolentseva[a], Andrey Simakov[a,*], Sergey Beloshapkin[b], Miguel Estrada[c], Eunice Vargas[d], Vladimir Sobolev[e], Roman Kenzhin[e], Sergio Fuentes[a]

[a] Universidad Nacional Autónoma de México, Centro de Nanociencias y Nanotecnología, Km. 107 Carretera Tijuana a Ensenada, C.P. 22860, Ensenada, Baja California, Mexico
[b] Materials and Surface Science Institute, University of Limerick, Limerick, Ireland
[c] Posgrado en Física de Materiales, Centro de Investigación Científico y de Educación Superior de Ensenada, C.P. 22860, Ensenada, B.C., Mexico
[d] Posgrado en Ciencias e Ingeniería, Área Nanotecnología, Universidad Autónoma de Baja California, Ensenada, B.C., Mexico
[e] Boreskov Institute of Catalysis, C.P. 630090, Novosibirsk, Russia

ARTICLE INFO

Article history:
Received 22 July 2011
Received in revised form 2 December 2011
Accepted 5 December 2011
Available online 13 December 2011

Keywords:
Gold
Nanoparticles
Ceria–alumina
Mixed oxides
Sol–gel
Transient analysis

ABSTRACT

Nanostructured ceria–alumina mixed oxides containing different concentrations of ceria (10 and 30 wt.%) were prepared by the sol–gel method using organo-metallic precursors of alumina and ceria. The size of alumina and ceria particles in the prepared Ce–Al–O mixed oxides was smaller than that of pure alumina or ceria. The gold catalysts (3 wt.% Au) supported on ceria–alumina mixed oxides by deposition–precipitation (DP) using $HAuCl_4$ and urea were characterized by several techniques: TEM, XPS and UV–vis spectroscopy, and temperature programmed reduction/oxidation (TPR/TPO). The catalytic activity of prepared $Au/CeO_2–Al_2O_3$ catalysts in CO oxidation was higher than that of Au/Al_2O_3 and Au/CeO_2 catalysts. Nanostructured ceria incorporated into an alumina matrix has been found quite effective for gold species activation in CO oxidation. In fact, transient analysis of CO oxidation provided an estimate of the relative content of (Au–ceria vacancy) active sites in catalysts. Obtained values are in good agreement with the order of activity for tested samples and gold dispersion according to EXAFS data.

Crown Copyright © 2011 Published by Elsevier B.V. All rights reserved.

1. Introduction

In the past decades highly dispersed gold nanospecies supported on various metal oxides have been reported to be active in many reactions including low temperature CO oxidation [1,2] and the water gas shift (WGS) reaction [3–5]. The catalytic activity of these gold catalysts strongly depends on the gold particle size, method of gold deposition, pretreatment conditions and nature of the supports [2]. The reducible support plays a decisive role in the formation and distribution of oxygen vacancies as well as in gold particle dispersion and shape, which are directly reflected on catalytic activity [2]. As a rule, gold nanoparticles supported on TiO_2, Fe_2O_3 [6], Co_3O_4 [7] or MgO [8] are active in CO oxidation.

Gold supported on nanocrystalline bulk ceria was recently found to exhibit excellent activity in CO oxidation [9–11] and the WGS reaction [12–14]. Deposition of ceria over porous materials is another way to prepare nanostructured ceria. As an example, application of alumina covered with ceria as support for gold catalysts drastically enhances the catalytic activity of gold species in CO oxidation, in comparison with gold catalysts supported on pure ceria or alumina [15]. Authors explained this effect by (i) the higher dispersion of gold on CeO_2/Al_2O_3 in contrast with the dispersion on Al_2O_3 and (ii) a strong promoting effect of ceria on the oxidation state of gold species. As previously shown [16], gold catalysts supported on alumina–ceria mixed oxides prepared by co-precipitation exhibit higher activity in the NO + CO reaction than gold supported on pure ceria. Similar tendencies were found for other noble metals supported on CeO_2/Al_2O_3 oxides [17,18]. On the other hand, highly active and stable gold catalysts were prepared for the WGS reaction by applying mixed ceria–alumina support, synthesized by mechano-chemical activation of the mixture of pure ceria and alumina [19]. However, mechano-chemical activation is less effective than co-precipitation [16] or the sol–gel technique [20,21] in increasing ceria dispersion. The synthesis of mixed oxides by sol–gel is well known to confer important structural, textural and chemical characteristics to noble metal catalysts, due to a better control of oxide–oxide interactions at the molecular scale. In addition, the sol–gel process permits to obtain highly homogeneous materials by incorporation of several components in a single-step synthesis [22]. Furthermore, application of the sol–gel technique enhances the formation of structural defects in oxides used as supports thus improving the catalytic activity [23].

* Corresponding author. Tel.: +52 646 174 46 02x360; fax: +52 646 174 46 03.
E-mail address: andrey@cnyn.unam.mx (A. Simakov).

0926-3373/$ – see front matter. Crown Copyright © 2011 Published by Elsevier B.V. All rights reserved.
doi:10.1016/j.apcatb.2011.12.010

The aim of the present work was to investigate the effect of ceria in nanostructured ceria–alumina mixed oxides prepared by sol–gel on the behavior of Au/Ce–Al–O catalysts in room-temperature CO oxidation.

2. Experimental

2.1. Sample preparation

Nanostructured Ce–Al–O mixed oxides with different content of ceria (10 and 30 wt.%) close to that in [15] were prepared by the sol–gel method from organo-metallic precursors following a procedure reported previously in [20,21]. A solution of cerium (III) 2,4-pentanedionate hydrate (Alfa-Aesar) in ethanol with moderate agitation was added to a mixture of aluminum sec-butoxide (Alfa-Aesar) in 2-methyl-2,4-pentanediol (Alfa-Aesar), left in reflux for 3 h with moderate agitation at 90 °C. Hydrolysis was attained by addition of deionized water. The obtained gel was aged for 10 h. Samples were dried under vacuum (about 10^{-3} Torr) at 100 °C for 12 h and then heated in an N_2 atmosphere up to 450 °C and maintained for 12 h, with a later treatment in O_2 at 650 °C for 4 h for decomposition of organic precursors.

Alumina prepared by sol–gel from organic precursors according to the procedure described above and commercial CeO_2 (Alfa-Aesar) were used as supports as well.

Gold (3 wt.%) was supported by deposition–precipitation using urea as a precipitation agent as in [24,25]. Four grams of support were added to 400 ml of an aqueous solution of $HAuCl_4$ (1.6×10^{-3} M) and urea (0.42 M). The initial pH of the solution was ~2. The suspension was vigorously stirred at 80 °C for 4 h. Then the suspension was filtered and washed with ammonium hydroxide (25 M) for 30 min. After stirring with ammonium hydroxide the pH of the solution was ~10. Finally, samples were washed in water until they reached pH 7, then filtered, and dried at room temperature for 24 h. The mixed support and catalyst samples are encoded as Ce(*N*)–Al and Au/Ce(*N*)–Al, where *N* (10 or 30) manifests ceria content (10 or 30 wt.%), respectively.

2.2. Sample characterization

The obtained gold samples were chemically analyzed with an inductively coupled plasma atomic emission spectroscopy (ICP-AES) using a Varian Liberty 110 ICP Emission Spectrometer. Typically, 30 mg of sample were dissolved in 20 ml of (H_2SO_4:HCl:HNO_3 = 6:6:3) acids and the sample was heated to 150 °C. The specific surface area of the samples was determined using the BET method by nitrogen thermal adsorption measurements in a Gemini 2600 Micromeritics device. Before analysis, samples were heated in Ar flow to 300 °C for 1 h.

X-ray diffraction (XRD) analysis was done with a Philips X'pert diffractometer equipped with a curved graphite monochromator applying Cu K_α (λ = 0.154 nm) radiation. Transmission electron microscopy (TEM) was performed with a JEOL 2010 Microscope. The sample was dispersed in isopropanol and dropped on a copper grid coated with carbon film. To determine the mean diameter of gold particles more than 200 particles were chosen. The mean diameter (d_m) of particles was calculated using the well-known procedure of particle size distribution histograms with the following formula: $d_m = \sum_i (x_i d_i)/\sum_i x_i$, where x_i is the number of particles with diameter d_i.

XPS data were obtained by a Kratos AXIS 165 spectrometer using monochromatic AlK_α radiation ($h\nu$ = 1486.58 eV) and fixed analyzer pass energy of 20 eV. All measured binding energies (BE) were referred to the C1s line of adventitious carbon at 284.8 eV. Spectrum deconvolution was done with background estimation using Shirley software.

UV–vis diffuse reflectance spectra (UV–vis DRS) were recorded at room temperature for gold samples treated in different gases (H_2, O_2 or He) with continuous temperature increase from 50 up to 350 °C with a ramp rate of 20 °C/min using a Varian Cary 300 Scan Spectrophotometer equipped with a standard diffuse reflectance unit. Teflon PTF Halon (Varian) was used as a reference. Each UV–vis DR spectrum presented below was obtained by subtraction of the fresh sample spectrum from the spectrum for the sample treated at different temperatures.

Temperature-programmed reduction (TPR), oxidation (TPO) and decomposition in helium flow (TPD) of freshly prepared gold samples were obtained under linear sample heating with a ramp rate of 20 °C/min up to 350 °C using gas mixtures 3% H_2 + He; 20% O_2 + He or 99% of pure helium, respectively, and in-line gas phase analysis with an HPR20 mass spectrometer (Hiden). The relative content of desorbed products was estimated taking into account all possible mass-fragments according to the Hiden mass-library, while hydrogen and oxygen uptake was calculated using reference gas mixtures.

FTIR spectrometer Nexus-760 with *in situ* cell from Harrick was used for DRIFT analysis of CO adsorbed at −40 °C. Before CO adsorption sample was pre-reduced *in situ* in flow of hydrogen (5 vol.%) diluted with helium with temperature increase up to 350 °C with ramp rate of 10 °C/min. Then sample in FTIR cell was purged with helium with simultaneous decrease of sample temperature to 25 °C. Further decrease of sample temperature up to −40 °C was carried out under evacuation with mechanical pump. The residual pressure was 10^{-3} Torr. The trap at −190 °C was used in order to avoid sample poisoning with oil vapor. CO adsorption (5 Torr) in the presence of oxygen (1 Torr) was performed at −40 °C. The FTIR spectra were recorded in K.M. units using MTC detector cooled by liquid nitrogen. The spectrum of sample before adsorption was used as a reference. All gases before entrance to FTIR cell were passed through a trap cooled at liquid nitrogen before admission to the IR cell. Gas phase components were controlled in line by HPR-20 mass spectrometer.

A catalytic activity test of CO oxidation at 25 °C was performed in a laboratory-made Pyrex flow reactor with gas mixture of UHP grade 1% CO + 0.5% O_2 + 0.5% Ar + He (80 ml/min) obtained by mixing pure components using massflow controllers (Matheson) and in-line mass spectroscopic analysis (HPR 20, Hiden). Residence time was about 10 g_{CAT} h mol CO^{-1}. Before the catalytic test, the catalyst was pre-reduced in hydrogen mixture (3% H_2 + He) or pre-oxidized in oxygen mixture (20% O_2 + He) with a temperature increase up to 350 °C with a ramp rate of 20 °C/min. Then the sample was purged by helium with a temperature decrease to 25 °C. Catalytic activity was expressed as value of CO consumed (mol) normalized on sample weight (g), surface gold atoms (mol) estimated from TEM or from EXAFS data. Carbon balance calculated as the CO consumed/CO_2 formed ratio was equal to 1 with the exception of the first ~15 s of contact of the reaction mixture with the catalyst bed. The CO, O_2 and CO_2 concentration were calculated using reference gas mixtures.

3. Results and discussion

3.1. Characterization of supports

3.1.1. X-ray diffraction

XRD patterns of the studied supports are presented in Fig. 1. The pattern of alumina is characterized by the presence of two-theta peaks at 36.9°, 45.8° and a more intense peak at 66.8° corresponding to the (2 2 2), (4 0 0) and (4 4 0) crystallographic planes, respectively. The XRD pattern of commercial ceria shows pronounced

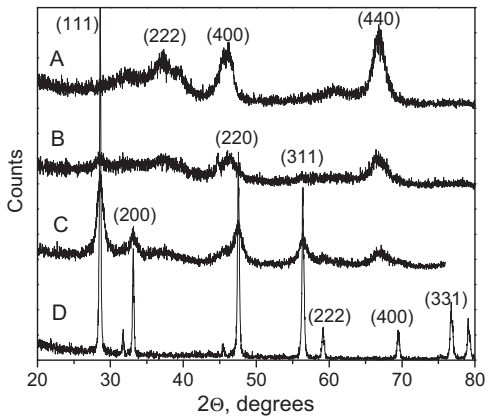

Fig. 1. XRD patterns of samples: (A) Al_2O_3, (B) Ce(10)–Al, (C) Ce(30)–Al and (D) CeO_2.

and narrow two-theta signals at 28.6°, 33.1°, 47.5°, 56.4°, 59.2°, 69.5°, 76.8° and 79.1°, which could be indexed to the (1 1 1), (2 0 0), (2 2 0), (3 1 1), (2 2 2), (4 0 0), (3 3 1) and (4 2 0) planes of the fluorite cubic ceria structure, respectively (see Fig. 1). The estimated size of ceria particles was about 43 nm. The value was obtained from the width of diffraction peak at 28.6° using Scherrer's formula. In XRD patterns of mixed oxides peaks were confirmed corresponding to alumina and ceria as well. Note that peak widths for mixed samples were different from those for individual oxides. An estimation of the size for alumina particles using the peak at 66.8° gave the following values: 6.4 nm, 5.5 nm and 5.1 nm for Al_2O_3, Ce(10)–Al and Ce(30)–Al samples, respectively. In turn, the size of ceria particles was about 3.2 nm and 9.0 nm for the Ce(10)–Al and Ce(30)–Al samples, respectively (Fig. 2). The ceria particles from the mixed oxides obtained in this work were smaller in size than those reported in [15] for ceria supported on alumina prepared by impregnation or for ceria mechano-chemically activated with alumina [19]. On the other hand, presently obtained values are comparable with the size (4–8 nm) of ceria–alumina mixed oxides prepared by co-precipitation [16] and by sol–gel [26,27].

Thus, the incorporation of ceria into the alumina matrix via the sol–gel method resulted in a decrease in ceria particle size but did not significantly affect the size of alumina particles. However, the introduction of ceria into alumina led to an increase in BET surface area of the mixed oxides in contrast with that for pure alumina (see Fig. 2).

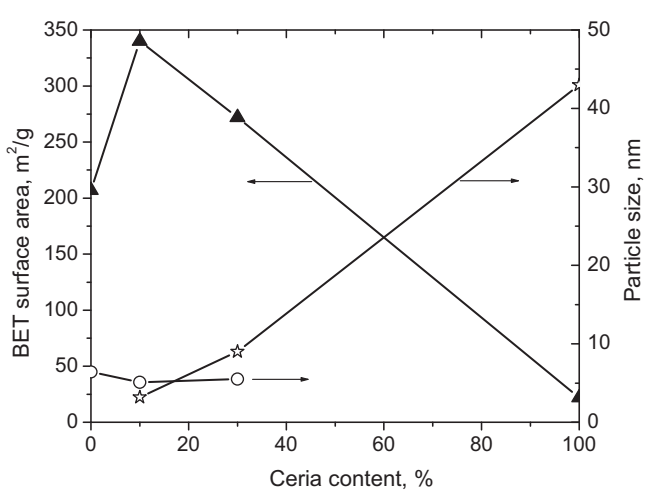

Fig. 2. The BET surface area (▲) and particle size of ceria (☆) and alumina (○) oxides estimated from peak width of CeO_2 (1 1 1) and Al_2O_3 (4 4 0) for CeO_2, Al_2O_3 and Ce(*N*)–Al samples.

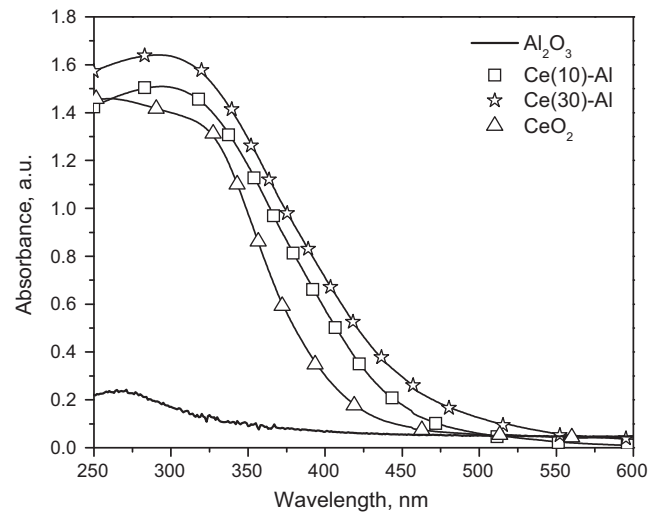

Fig. 3. UV–vis DR spectra of studied supports.

3.1.2. UV–vis DR spectra

Fig. 3 shows the UV–vis DR spectra of prepared supports. Pure alumina displayed an absorption band at around 260 nm, likely due to the presence of structural defects in the sol–gel material [20]. The UV–vis DR spectra for CeO_2 and Ce–Al samples were similar to each other and showed adsorption starting at around 500 nm [28]. The DR spectra of the samples after Kubelka–Munk treatment are shown in Fig. 4. The intersection between the linear fit and the photon energy axis gives the value of the band-gap energy (E_{gap}) according to the procedure described in [29]. The value for band-gap energy of the commercial ceria sample was estimated as 3.55 eV. It is well known that the value of the band-gap energy for ceria depends on sample preparation and size of ceria crystals. Ultra fine ceria particles of about 5 nm in size are characterized by band-gap energy equal to 3.0 eV [30]. On the other hand, the ceria nanoparticles of 2.6 and 4.1 nm synthesized by the microemulsion method reveal different values of band-gap energy (3.44 and 3.38 eV, respectively) [31]. The band-gap energy for ceria nanocrystals of 2.6–6.9 nm is estimated at around 3.4 eV in [32]. As shown in [27] ceria–alumina supports prepared by sol–gel from inorganic precursors with ceria particles of 3.2 and 2.1 nm are characterized by band-gap energy values of 2.92 and 3.00 eV, respectively.

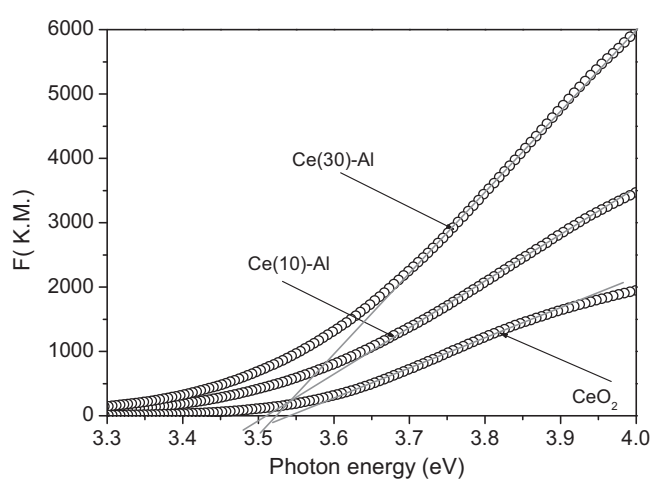

Fig. 4. UV–vis spectra of studied supports transformed in Kubelka–Munk function.

However, the Ce(10)–Al and Ce(30)–Al samples prepared in this work revealed similar values of band-gap energy equal to 3.51 and 3.52 eV respectively, comparable with the value for commercial ceria which is 3.55 eV, in contrast with the drastic difference in ceria particle size for the mentioned samples. The ceria–alumina interaction may affect the value of the band-gap energy, because ceria in Ce–Al–O mixed oxides is mostly embedded into alumina.

3.2. Characterization of catalysts

During the deposition–precipitation procedure changes in color intensity of gold solutions were observed. The initial bright-yellow color changed to an inconspicuous yellow, the rate of change being dependent on the support. As a rule, these changes were faster for the samples including ceria than with pure alumina because of the more rapid anchoring of gold species on ceria than on alumina. Among other important factors that must be taken into account during the preparation of gold catalysts is the isoelectric point (IEP) of the supports [33]. The IEP of alumina and ceria used in this work was approximately 7–8 and 6.7–8.6, respectively. Mixed oxides may exhibit IEP values intermediate to those of the corresponding pure oxides [34]. Indeed, according to [15], CeO_2/Al_2O_3 mixed oxides show an IEP equal to 8.14. The pH value for the final solution was about 8 after 4 h of gold deposition. This value is closer to the IEP of ceria. Therefore, it is possible to expect a more complete deposition of gold hydroxide species on ceria rather than on alumina [33].

3.2.1. TEM analysis

The gold particle size distribution for samples treated in different media (H_2 or O_2) estimated from TEM images is presented in Fig. 5. 15 micrographs were taken for each sample in order to make estimation well because of low contrast between ceria and gold in TEM. More than 200 particles were measured for each sample. The average particle size depends on both the support used and the nature of the gases used for sample treatments. The gold metal particles were formed due to both chemical reduction and thermal decomposition of the gold precursor. In addition, according to our data obtained with mass-spectrometry, chemical reduction of the gold precursor proceeded through interaction with hydrogen and/or with other reducing compounds (urea, ammonia), which were present on the sample surface due to the preparation procedure (data will be presented in Section 3.2.3). Metal gold particles may be expected to form more rapidly at low temperature under reduction than under oxidation, in particular on inert supports. Indeed, for non-reducible supports such as alumina, pretreatment conditions of the sample dramatically affected gold particle size, while gold metal particles supported on reducible oxides such as ceria were approximately of the same diameter if either reduced or oxidized. The latter could be explained by a stronger chemical interaction of gold species with ceria than with alumina. In the case of reducible supports such as ceria there is one more type of gold species interaction with the support which should be taken into account [35]. As described in [36], freshly formed metal gold species strongly interact with the vacancies in partly reduced ceria. In turn, partial reduction of ceria may be catalyzed in the presence of gold species on the ceria surface as observed in [12,13,35] and this was also shown experimentally in our work (data will be presented below).

In the case of mixed oxides non-uniform distribution of particle size was observed probably due to the interaction of gold species with both alumina and ceria. Indeed, reduced and oxidized

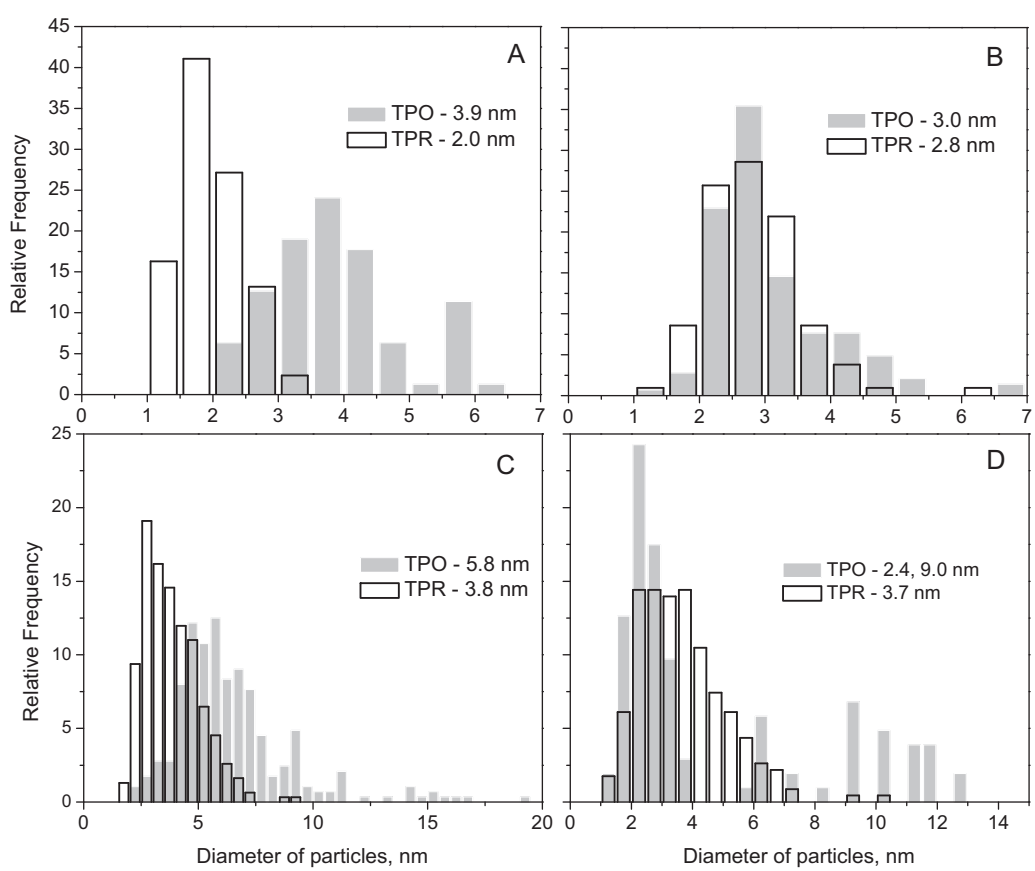

Fig. 5. Gold particle size distribution for gold including samples heated at 350 °C in hydrogen (TPR) and in oxygen (TPO) according to TEM analysis: (A) Au/Al_2O_3, (B) Au/CeO_2, (C) Au/Ce(10)–Al and (D) Au/Ce(30)–Al.

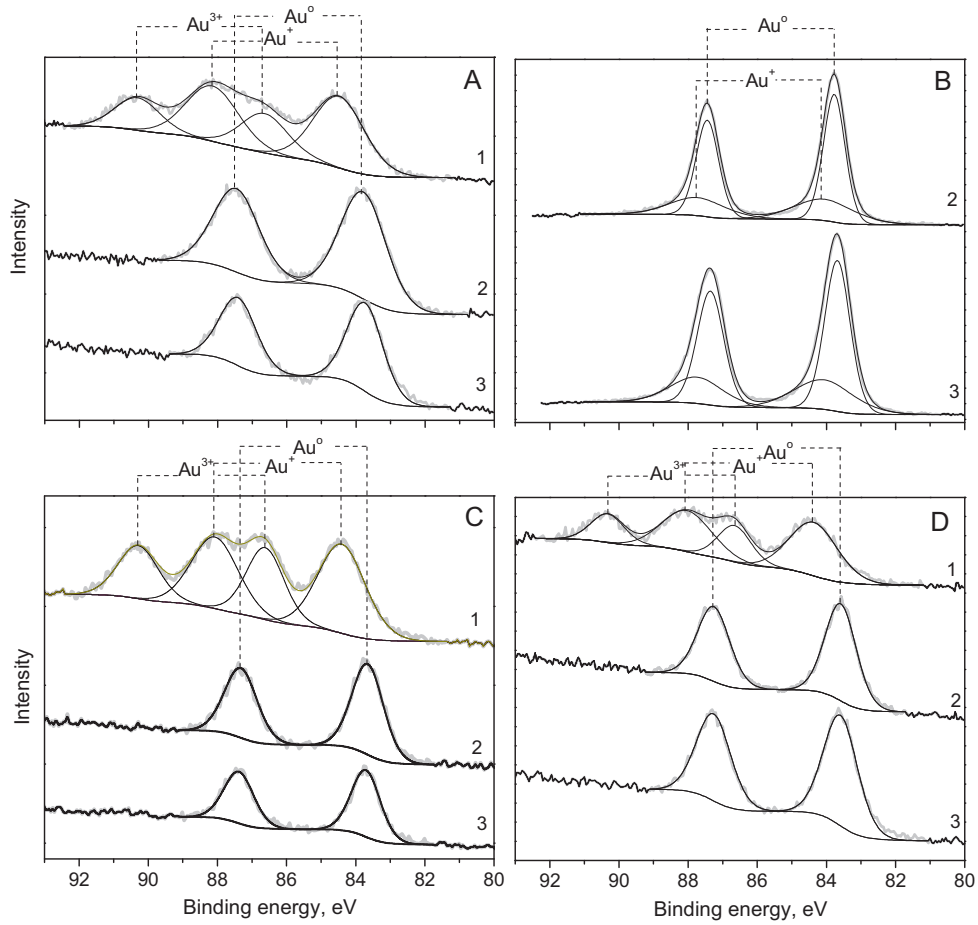

Fig. 6. Au 4f XPS spectra of samples: (A) Au/Al_2O_3, (B) Au/CeO_2, (C) Au/Ce(10)–Al and (D) Au/Ce(30)–Al. XPS spectra presented for untreated samples (1), samples calcined in oxygen at 350 °C (2) and reduced in hydrogen at 350 °C (3).

Au/Ce–Al samples displayed a bimodal distribution of gold metal particles.

3.2.2. XPS analysis

The XPS spectra of gold catalysts either untreated or heated in oxygen or in hydrogen at 350 °C are presented in Fig. 6. The Au 4f spectra, characterized by the two spin-orbit components, Au $4f_{7/2}$ and Au $4f_{5/2}$ separated by 3.67 eV, exhibited three doublets attributed to different gold species. The curve fitting of spectrum Au 4f indicates Au $4f_{7/2}$ components at BE value around 83.8; 84.5 and 86.6 eV, which can be attributed to Au^0, Au^+ and Au^{3+} according to [37–39]. Note that untreated gold catalysts were characterized by the presence of cationic gold species (Au^+ and Au^{3+}). No metallic gold species were found in these samples, which is in good agreement with our EXAFS analysis of these samples presented in [40,41]. It is shown that the gold catalysts supported on nanostructured Ce–Al–O mixed oxides are characterized with the presence of Au^{3+} species only located on the support surface in slightly disordered octahedral oxygen coordination even after sample heating at 150 °C. The following distances and coordination numbers are $R_{Au-O} \sim 1.99$ Å, CN ~ 5.6–5.8; $R_{Au-O-Al} \sim 3.06$ Å, CN ~ 2.2–2.3; $R_{Au-O-Au} \sim 3.69$–3.72 Å, CN ~ 2.1–2.3. The high coordination number for gold cations in these samples, when calcined even at 150 °C, displayed high stability of gold cations due to the preparation procedure. Indeed, sample washing with concentrated ammonia solution results in the stabilization of cationic gold species [42]. The presence of Au^+ cations detected in XPS spectra of freshly prepared samples may be explained by partial distortion/decomposition of gold hydroxide in the high vacuum XPS chamber; this was also observed in [43]. The FWHM values of Au^{3+} species for untreated Au/Ce(*N*)–Al samples (see Table 1) were low in contrast with those for Au/Al_2O_3, which also correlates with the higher relative content of Au^+ presented on pure alumina than on mixed oxides. These data manifested the stronger gold hydroxide distortion on pure alumina than on mixed oxides.

Table 1
XPS data of Au $4f_{7/2}$ binding energies values, eV referred to as C 1s (284.8 eV) for studied samples.

Sample	Type of sample pretreatment		
	Untreated	Oxygen	Hydrogen
Au/Al_2O_3	Au^+(84.5; 1.7) Au^{3+}(86.6; 1.6)	Au^0(83.8; 1.5)	Au^0(83.7; 1.2)
Au/CeO_2	–	Au^0(83.8; 0.7)Au^+(84.1; 2.04)	Au^0(83.7; 0.9)Au^+(84.1; 2.04)
Au/Ce(10)–Al	Au^+(84.4; 1.6)Au^{3+}(86.6; 1.3)	Au^0(83.6; 1.1)	Au^0(83.7; 1.0)
Au/Ce(30)–Al	Au^+(84.4; 1.6)Au^{3+}(86.7; 1.1)	Au^0(83.6; 0.9)	Au^0(83.6; 1.1)

In parentheses shown the peak position of Au species and the full width at half maximum (FWHM).

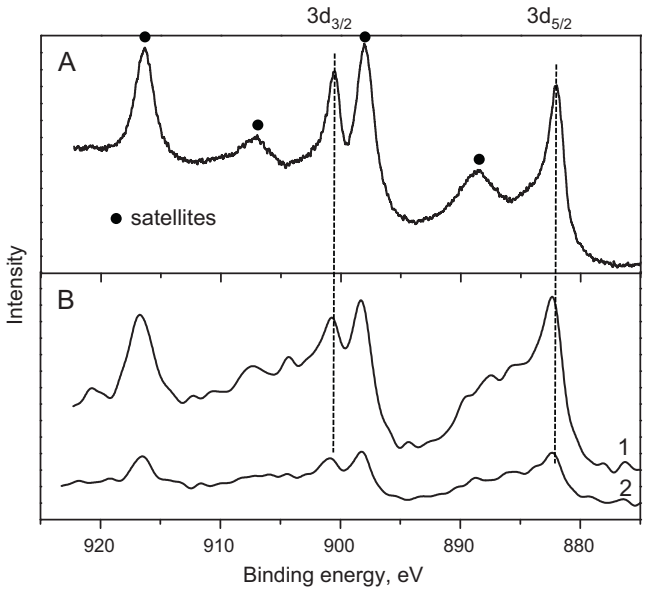

Fig. 7. Ce 3d XPS spectra for Au/CeO_2 (A) and Au/Ce(*N*)–Al (B) samples. Curve 1 – Au/Ce(10)–Al, curve 2 – Au/Ce(30)–Al.

The reduction or oxidation of Au/Al_2O_3, Au/Ce(10)–Al and Au/Ce(30)–Al samples led to the formation of metallic gold species only (Fig. 6A, C and D). EXAFS analysis of these samples [41] reveals the following distances and coordination numbers: $R_{Au-Au} \sim 2.82–2.84$ Å, CN ~ 5.8–6.3. According to XPS data some portion of Au^+ cations was still present in oxidized and even in reduced Au/CeO_2 samples (Fig. 6B). The high FWHM value for Au^+ cations in the treated Au/CeO_2 sample compared with the data for untreated samples implied that these cations were formed within the thin layer probably located in the gold–ceria interface as was also mentioned in [36,43]. The absence of such species in the catalysts based on mixed oxides could be caused by the low content of ceria.

The XPS spectra of Ce 3d for samples Au/CeO_2 and Au/Ce(*N*)–Al are pictured in Fig. 7. Two components of Ce $3d_{5/2}$ and Ce $3d_{3/2}$ separated by 18.5 eV were observed. The peaks in the spectra with satellite lines (marked in the figure) correspond to Ce^{4+} in CeO_2 [37]. The XPS spectra for both bulk ceria and ceria–alumina mixed oxides were practically the same. However, the intensity of the spectra for the mixed oxides was low in contrast with bulk ceria, probably due to the low concentration of ceria in mixed oxides. The noticeable changes in the XPS spectra of the Ce 3d region were not found in untreated gold catalysts or after reduction in hydrogen and calcination in oxygen (figure not shown).

3.2.3. TPR and TPO data

Transformation under reduction or oxidation of gold species supported on different supports was studied by TPR with hydrogen or by TPO with oxygen. The typical TPR and TPO profiles for the Au/CeO_2 sample are shown in Fig. 8. The in-line analysis of the gas phase products with mass-spectrometer during the TPR/TPO experiment allowed to detect not only hydrogen or oxygen uptake with a sample temperature increase but desorption of water, CO_2, ammonia and nitrogen oxides. Some portion of desorbed water and CO_2 could be caused by removal of these compounds from the sample being pre-exposed to air. In addition, simultaneous desorption of water, CO_2 and nitrogen within the temperature interval of 75–200 °C could also correspond to thermal decomposition of urea or its reaction with gold hydroxide. Urea can be present on the sample surface due to its intercalation into gold hydroxide particles as described for nickel hydroxide particles in [44]. Hydrogen uptake occurred within the temperature interval of 200–250 °C (Fig. 8A) with formation of gold metal particles (see section UV–vis data). Any hydrogen uptake was observed on bare supports in 25–350 °C temperature interval (data not shown here). Hydrogen consumption was accompanied with desorption of ammonia and of the products of its oxidation. Ammonia seems to have been adsorbed on the sample surface during sample washing with ammonia aqueous solution. In addition, some portion of ammonia could have been formed due to thermal decomposition of urea within the temperature interval of 75–200 °C. Ammonia desorption seems to be caused by transformation of cationic gold species, which strongly interact with ammonia, into metallic gold species, which were characterized by low affinity with ammonia. Indeed, ammonia desorption was observed exactly at the same temperature interval as hydrogen consumption. Experimentally measured hydrogen uptake for the Au/CeO_2 catalyst exceeded the amount required for the reduction of only the gold precursor. Hydrogen uptake estimation revealed that in addition to gold species reduction, partial reduction of ceria also occurred, which has also been observed in [5,12,13,45]. In addition to gold species reduction with hydrogen, reduction with ammonia takes place too. As an example, desorption of nitrogen and nitrous oxide evidences that ammonia oxidation proceeded even in a hydrogen atmosphere. Appearance of the ammonia oxidation products under such conditions may be explained by the reaction of ammonia with an oxidant such as gold hydroxide. Indeed, in the TPO profile the amount of nitrogen oxides and nitrogen was higher than that in the TPR profile because ammonia oxidation occurred by gas phase oxygen as well. Note that the temperature interval of

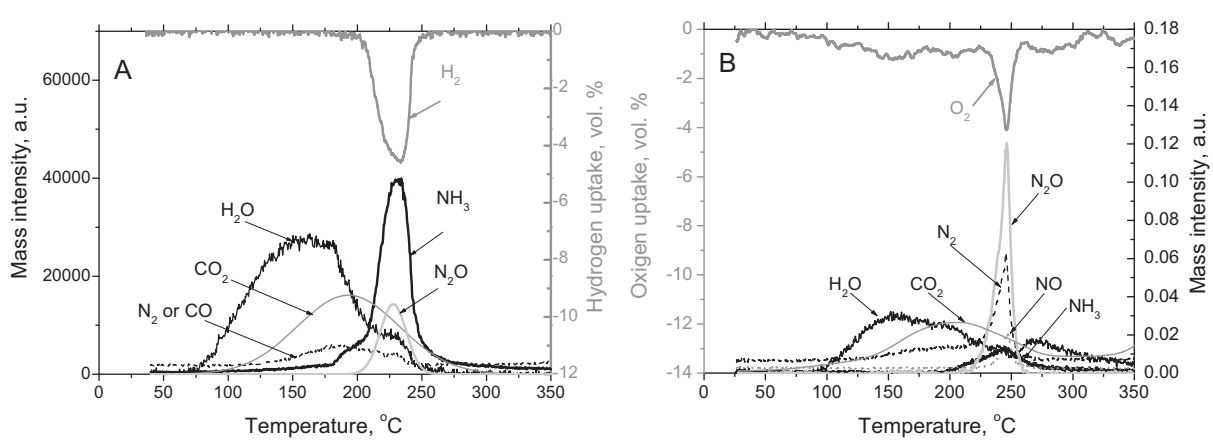

Fig. 8. TPR (A) and TPO (B) profiles for Au/CeO_2 catalyst.

oxygen consumption coincided with that for ammonia oxidation products (see Fig. 8B).

Similar TPR and TPO profiles were obtained for all studied samples. The temperature interval of gold precursor thermal decomposition with desorption of CO_2 and water (75–200 °C) and its reduction with formation of metallic gold species and desorption of ammonia and products of its oxidation (200–250 °C) was similar for TPR and TPO experiments, while the relative contribution of desorbed products was different.

Note that hydrogen uptake was observed at temperature higher than that for similar catalytic systems prepared by co-precipitation or mechano-chemical activation [19,35,46,47]. Samples prepared in the current work were thoroughly washed with ammonia aqueous solution, in contrast with those described in the literature. Elimination of chlorine with ammonia solution from the sample surface probably resulted in high stabilization of gold species, which was also described in [42]. On the other hand, Ce–Al–O mixed oxides prepared by the sol–gel technique were characterized by fine distribution of components and relatively high content of structural defects, which can interact with gold species strongly.

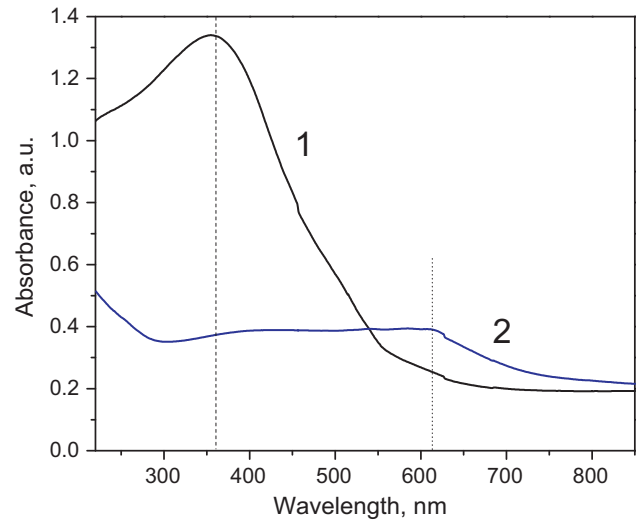

Fig. 9. UV–vis spectra of $Au(OH)_3$ samples prepared by hydrolysis of aqueous solution of $HAuCl_4$ with NH_4OH (curve 1) and with $NaHCO_3$ (curve 2) at room temperature.

3.2.4. UV–vis DR spectra

UV–vis DR spectra for gold hydroxide as reference sample prepared by two different routes are shown in Fig. 9. The sample prepared via hydrolysis of $HAuCl_4$ with NH_4OH showed a characteristic band at around 360 nm which could be assigned to the band of charge transfer (BCT) between gold and oxygen (dotted line), and was previously described in [48,49]. In the spectrum of the sample prepared with $NaHCO_3$, in addition to the BCT there was adsorption at around 600 nm (dashed line). The latter band may be assigned to the surface plasmon peak for gold metal particles [50,51]. The red shift of the plasmon peak position from 520 to 600 nm seems to be caused by gold nanoparticles located inside $Au(OH)_3$ crystals, which have a different dielectric function as that for air [52]. Note that when $HAuCl_4$ was hydrolyzed with $NaHCO_3$ in contrast with NH_4OH, partial reduction of the gold species took place.

UV–vis DR spectra for fresh samples and for samples thermally treated with different gases within the temperature range of 50–350 °C are shown in Figs. 10–13. The spectra for fresh samples were characterized by an adsorption band at around 380 nm. Coincidence of the band position for the fresh Au/Al_2O_3 catalyst and massive gold hydroxide indicates that this band could be ascribed to the BCT band between gold and oxygen due to the presence of gold hydroxide species. It is in a good agreement with our EXAFS data for these samples [41]. The distance Au–O (1.99 Å) found for samples heated up to 150 °C is close to that in gold hydroxide in contrary with data obtained in [25]. Difference in the EXAFS parameters found for gold deposit in [41] and in [25] could be explained by different duration of DP procedure (4 h and 16 h, respectively), which do affect strongly on the structure of gold deposit.

The temperature rise up to 150 °C led to an increase in BCT intensity, which could be explained by the further structural transformations of gold hydroxide. Indeed, desorption of CO_2 and water as the products of gold precursor thermal decomposition were detected within this temperature interval both in the TPR and TPO profiles (Fig. 8). Note that the BCT intensity increase was most pronounced in the spectra for reduced Au/Ce(10)–Al and Au/Ce(30)–Al samples (see Figs. 11 and 12, respectively).

The UV–vis DR spectra of all samples drastically changed after treatments with hydrogen, helium or oxygen at temperatures above 200 °C with the appearance of a plasmon band within the 530–620 nm interval. The changes in the spectra at temperatures below 200 °C depended on the nature of the support, being more pronounced for the Au/Al_2O_3 sample, and on the treatment of the sample. As a rule, reduced samples were characterized by a more rapid increase of plasmon peak intensity than samples after treatment with oxygen or helium (see Figs. 10–13). The beginning of gold nanoparticle formation coincided with the onset of hydrogen uptake according to the TPR profiles shown in Fig. 8.

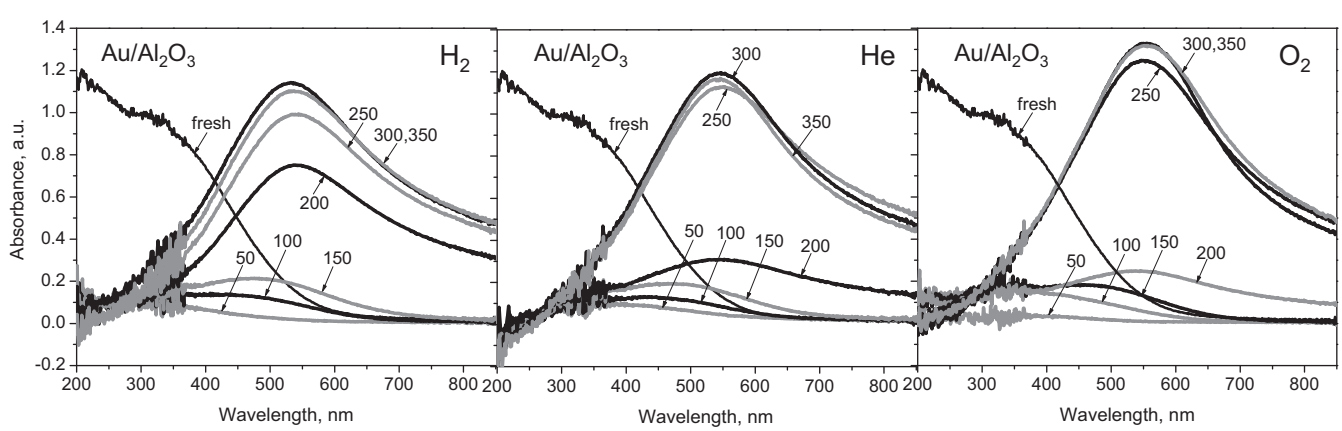

Fig. 10. UV–vis spectra of Au/Al_2O_3 catalyst vs temperature of treatment in hydrogen, helium and oxygen, respectively. Temperatures of treatments are pictured for each spectrum.

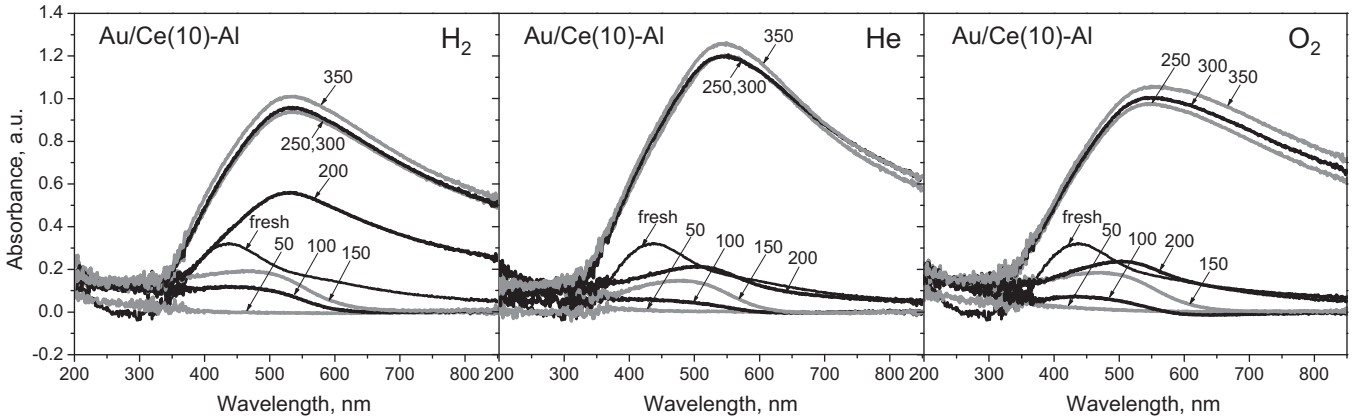

Fig. 11. UV–vis spectra of Au/Ce(10)–Al catalyst vs temperature of treatment in hydrogen, helium and oxygen, respectively. Temperatures of treatments are pictured for each spectrum.

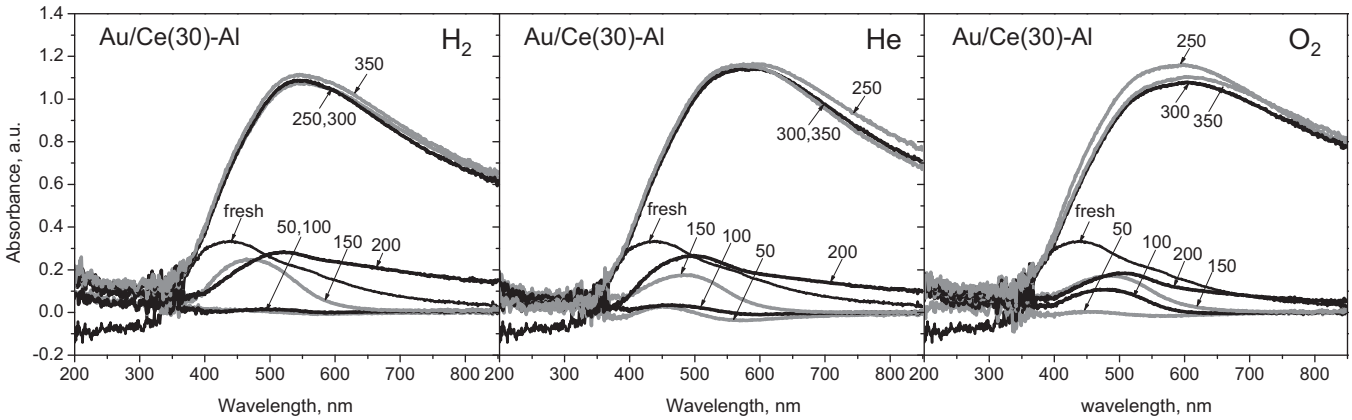

Fig. 12. UV–vis spectra of Au/Ce(30)–Al catalyst vs temperature of treatment in hydrogen, helium and oxygen, respectively. Temperatures of treatments are pictured for each spectrum.

No drastic changes in the UV–vis DR spectra of all samples were observed in the temperature interval of 250–350 °C (Figs. 10–13) which correlates well with the TPR, TPD and TPO data. According to the TPR/TPO experiments, hydrogen/oxygen uptake was practically finished at 250–270 °C and no products were desorbed to the gas phase.

The position of the plasmon peak in UV–vis spectra for samples after different treatments is presented in Table 2. A red shift of the plasmon peak was observed in UV–vis spectra with increasing ceria relative content in the samples (see Table 2). The position of the plasmon peak may depend on various factors: (i) the dielectric function of the medium surrounding the particles, ε_0, and (ii) gold particle size, as described in [52]. However, no correlation was observed between average particle size and position of the plasmon peak. Therefore, for these samples the position of the plasmon peak may primarily depend on the dielectric properties of the medium

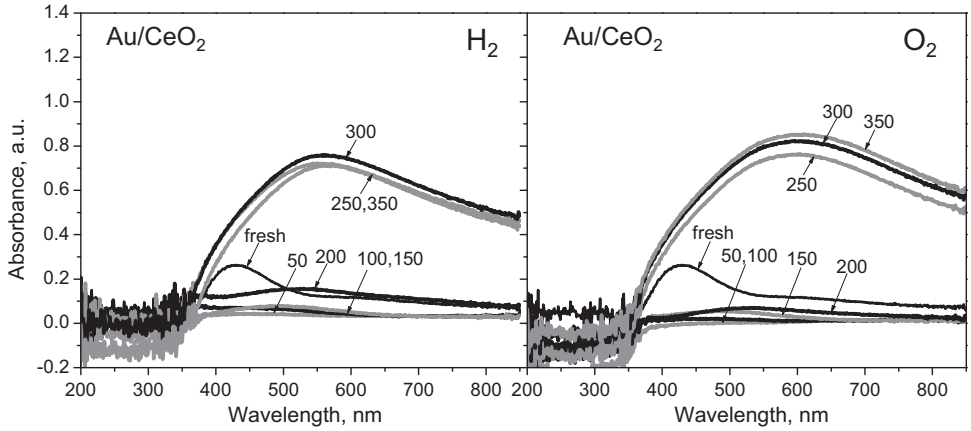

Fig. 13. UV–vis spectra of Au/CeO_2 catalyst vs temperature of treatment in hydrogen and oxygen, respectively. Temperatures of treatments are pictured for each spectrum.

Table 2
Position of plasmon peak (Au^0) according to UV–vis data.

Catalysts	Plasmon peak (Au^0), nm		
	Reduced sample	Sample treated in He	Oxidized sample
Au/Al_2O_3	534	543	550
Au/CeO_2	562	–	605
Au/Ce(10)–Al	529	544	554
Au/Ce(30)–Al	540/600	540/605	548/619

surrounding the gold metal particles. Indeed, for samples based on mixed oxides two plasmon peaks were observed, particularly for Au/Ce(30)–Al, which could be explained by the presence of gold particles stabilized both on alumina and ceria surface sites (see Table 2 and Fig. 12).

3.3. FTIR spectra of CO adsorbed on pre-reduced catalysts

The FTIR spectra collected during $CO + O_2$ adsorption at −40 °C on pre-reduced Au/Al_2O_3 and Au/Ce(30)–Al catalysts are illustrated in Fig. 14 (left and right), respectively. $CO + O_2$ adsorption on Au/Al_2O_3 catalyst led to the appearance of peak centered at 2105 cm^{-1}, which was assigned to CO adsorbed on Au^0 step sites on metallic gold nanoparticles according to [53–56]. The further CO adsorption resulted in the peak red shift to 2103 cm^{-1} as it was also found in [53,54]. Similar peak centered at 2105 cm^{-1} was observed on Au/Ce(30)–Al catalyst at the beginning of $CO + O_2$ adsorption. Thus, only metallic gold species were found on the surface of both pre-reduced samples. The difference in intensity of this peak for these two catalysts seems to be referred to higher content of well dispersed metallic gold species on Ce–Al–O mixed oxides rather than on pure alumina. In contrast to Au/Al_2O_3 sample $CO + O_2$ adsorption on Au/Ce(30)–Al sample led to the appearance of other two peaks with low intensity at 2343 cm^{-1} and 2170 cm^{-1}. According to [53,56] these peaks were assigned to CO_2 and CO adsorbed on the support surface, respectively. Appearance of CO_2 implies that CO was oxidized partly over Au/Ce(30)–Al catalyst even at −40 C. During further adsorption the peak centered at 2152 cm^{-1} was observed. Similar peak found in [53,56] was referred to CO adsorption on Au^{1+} cationic gold species. One can see that appearance of cationic gold species was accompanied with remarkable increase of CO_2 peak intensity (Fig. 14, right). Therefore, formation of CO_2 was accelerated dramatically in the presence of cationic gold species.

The data obtained by FTIR of CO adsorbed are in a good agreement with model of CO oxidation over gold catalyst supported on reducible oxides [2]. According to that model reducible support plays key role in the oxygen activation on its vacancies located close to gold species. Adsorption of oxygen on these sites results in the formation of activated oxygen species with partial charge transfer from nearest gold species and creation of positively charged gold species. Indeed, in contrast to Au/Al_2O_3 catalyst pre-reduced ceria including catalysts are characterized with the presence of partly reduced ceria species according to our TPR data mentioned above and those described in the literature [5,12,13,45]. Remarkable increase of CO_2 formation in the presence of cationic gold species manifests the key role of redox transformations in the system "metal gold species – ceria oxygen vacancy" to "cationic gold species – activated oxygen species".

3.4. CO oxidation test

Results of catalytic activity in CO oxidation at room temperature on gold catalysts after different treatments are shown in Fig. 15. The nature of the supports and the pretreatment (O_2 or H_2) of catalysts drastically affected the activity of samples. The gold catalysts supported on single oxides such as alumina and ceria were characterized by a relatively low activity, in contrast with gold supported on Ce(*N*)–Al mixed oxides (see Fig. 15). In addition, the activity level strongly depended on the pretreatment of ceria-including catalysts in contrast with the Au/Al_2O_3 sample (see Fig. 15). The level of activity for Au/Al_2O_3 catalyst after

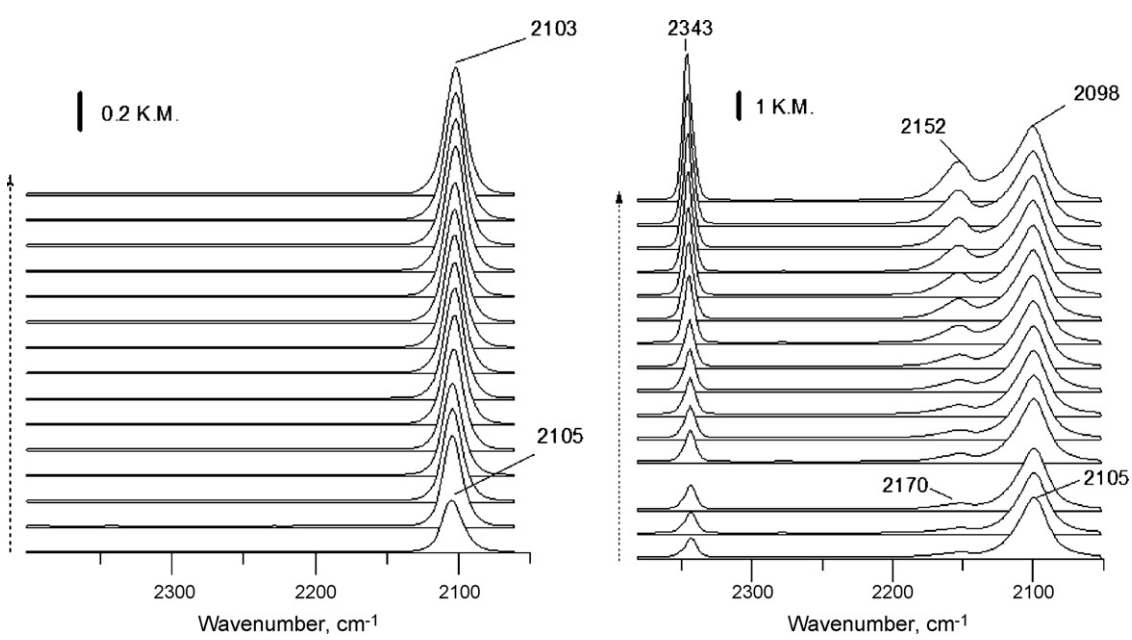

Fig. 14. FTIR spectra of CO adsorbed at −40 °C on pre-reduced Au/Al_2O_3 (left) and Au/Ce(30)-Al (right) samples. Spectra were collected each 15 s.

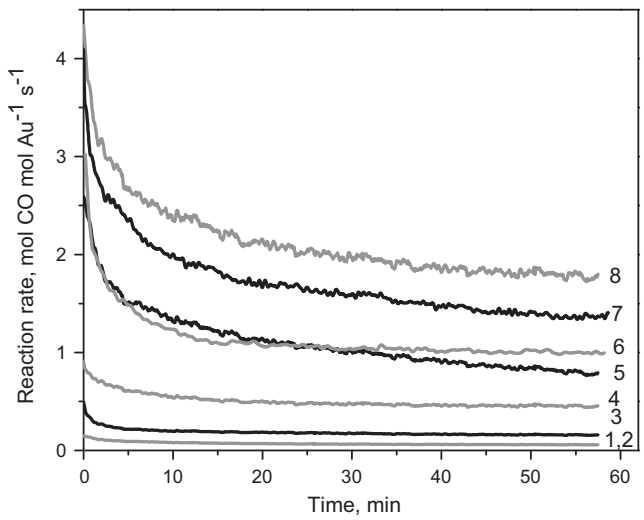

Fig. 15. Reaction rate of CO oxidation at room temperature over catalysts after different pretreatments: (1) Au/Al_2O_3–TPR, (2) Au/Al_2O_3–TPO, (3) Au/CeO_2–TPR, (4) Au/CeO_2–TPO, (5) Au/Ce(10)–Al–TPR, (6) Au/Ce(30)–Al–TPR, (7) Au/Ce(30)–Al–TPO, (8) Au/Ce(10)–Al–TPO. The reaction rate was calculated with proposition that only gold atoms located on the surface of gold metal particles are participating in the reaction.

treatments in hydrogen and oxygen (curves 1 and 2, respectively) was practically equal. The highest activity was observed for preoxidized ceria including samples. Obtained values of catalytic activity (0.22–1.95 mol CO mol Au^{-1} s^{-1}) were characterized by a higher order of magnitude than those reported in [57] for Au/CeO_2 (0.056 mol CO mol Au^{-1} s^{-1}), for gold catalysts supported on ceria prepared as nanorods (0.045 mol CO mol Au^{-1} s^{-1}) [58] and for gold supported on CeO_2–Al_2O_3 mixed oxides prepared by impregnation of alumina with ceria precursor (0.019 mol CO mol Au^{-1} s^{-1}) [15]. Another frequent way to express catalytic activity is the value of CO consumption normalized on catalyst weight. Values obtained in the current work (6.82×10^{-6}–3.42×10^{-4} mol CO s^{-1} g_{cat}^{-1}) are comparable or higher than those for Au/CeO_2 (1.2×10^{-6}–7.4×10^{-6} mol CO s^{-1} g_{cat}^{-1}) reported in [9,59–61]. Taking into account the value of the coordination number for Au atoms in the Au/Ce(*N*)–Al sample (about 6) measured in [41], dispersion of gold species could be estimated by about 50% using the correlation between the coordination number and gold dispersion found for supported gold nanoparticles in [62]. Therefore, the catalytic activity of Au/Ce(*N*)–Al samples could be more exactly estimated in terms of the CO consumed normalized on 50% of all gold atoms in the studied catalysts. These values presently obtained for Au/CeO_2 supported on commercial ceria (0.044–0.103 mol CO mol Au^{-1} s^{-1}) are comparable with the literature data for a similar system, while values for Au/Ce(*N*)–Al catalysts (0.15–0.21 mol CO mol Au^{-1} s^{-1}) supported on nanostructured mixed oxides prepared by sol–gel are higher than those presented in the literature.

The difference in activity of gold catalysts supported either on pure oxides (ceria or alumina) or on ceria–alumina mixed oxides may be explained after transient analysis of the reaction mixture in contact with sample. The concentration profiles obtained for CO, CO_2 and oxygen on different pre-reduced catalysts after the switch from helium to the reaction mixture are presented in Fig. 16. Curves are marked as CO^{out}, CO_2 and O_2^{out}. For comparison, concentration profiles of CO and oxygen incoming into the reactor are also pictured as CO^{in} and O_2^{in} curves, respectively. Later profiles were simulated using an argon profile as a tracer, like in [63,64]. For

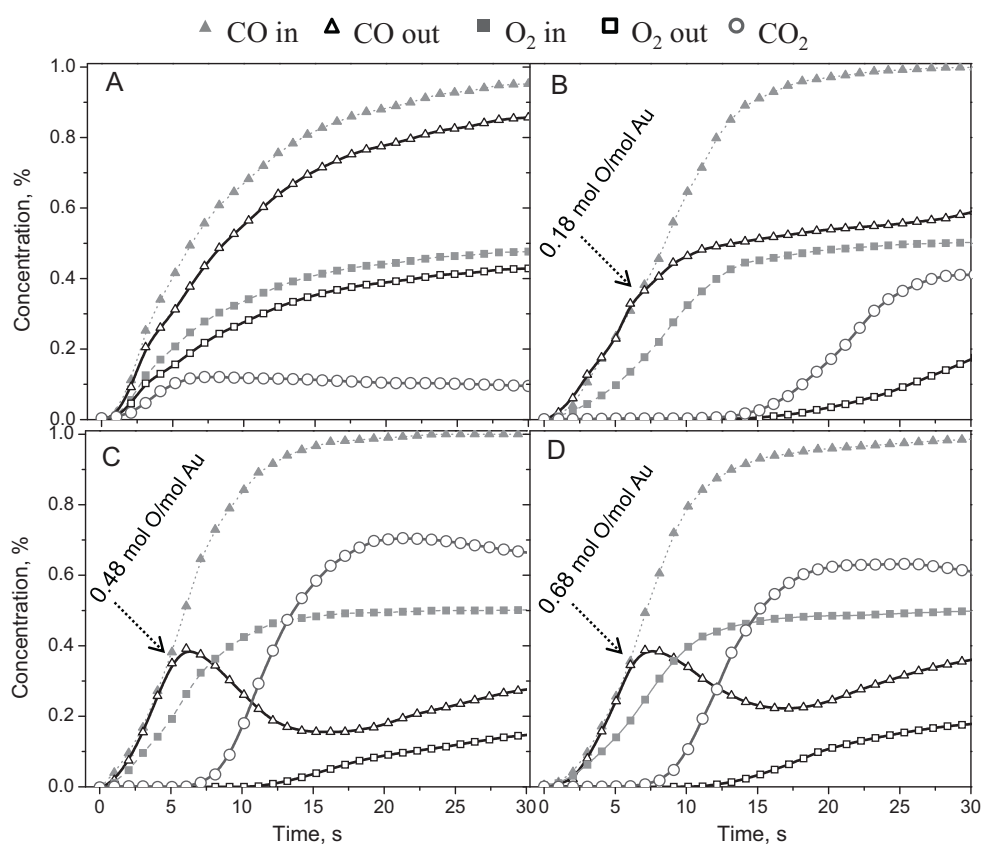

Fig. 16. CO, CO_2 and O_2 profiles during switch from helium to reaction mixture at 25 °C over catalysts prereduced *in situ* in hydrogen: (A) Au/Al_2O_3, (B) Au/CeO_2, (C) Au/Ce(10)–Al and (D) Au/Ce(30)–Al.

all ceria-containing catalysts there was an induction period during that CO initially did not react with the catalyst, which is illustrated by the similarity CO^{in} and CO^{out} curves (Fig. 16B–D). However, there is a large difference for the oxygen curves, which indicates oxygen consumption. Only after adsorption on the catalyst of a definite portion of oxygen, CO consumption started with CO_2 formation (see arrows in Fig. 16B–D). The *in situ* reduced catalysts contained only metallic gold species characterized by lower CO oxidation activity than oxidized gold species [10,43]. In order to start CO oxidation, metallic gold species must be activated by oxygen (see Section 3.3). The oxygen adsorption onto ceria vacancies formed under catalyst pre-reduction in hydrogen, located close to the gold metallic species, resulted in the formation of oxygen species and positively charged gold species active in CO oxidation. Estimated values of oxygen adsorbed before the start of the reaction (arrow in Fig. 16) were equal to 0.18 mol O/mol Au for Au/CeO_2, 0.48 mol O/mol Au for Au/Ce(10)–Al and 0.68 mol O/mol Au for Au/Ce(30)–Al. It should be emphasized, that these values are close to the values of gold dispersion according to EXAFS data obtained for these catalysts in [40,41]. All ceria-including catalysts showed the delay in appearance of CO_2 in the gas phase. It could be assigned to well known effect of strong CO_2 chemisorption on reduced ceria [65,66]. Amount of CO_2 adsorbed was estimated by calculation of carbon balance. After catalytic activity test samples were heated with the ramp rate of 20 °C/min up to 350 °C in He flow. Quantity of CO_2 desorbed coincided well with that adsorbed during first 15 s of sample contact with reaction mixture. In the case of the Au/Al_2O_3 catalyst, CO_2 was formed immediately with simultaneous consumption of both CO and oxygen. However, the level of activity for Au/Al_2O_3 was much lower probably due to the difficulty of oxygen/gold activation in the ceria-free system (Fig. 16A). Obtained values of adsorbed oxygen may be considered an estimate of the relative content of (Au–ceria vacancy) active sites in catalysts, and these values are in good agreement with the order of activity for tested samples and gold dispersion according to estimations based on EXAFS data.

4. Conclusions

Nanostructured ceria–alumina mixed oxides with different content of ceria prepared by sol–gel technique from organo-metallic precursors were more effective in the formation of catalytically active gold species for CO oxidation compared with similar oxides prepared by other techniques such as co-precipitation or mechano-chemical activation. The incorporation of ceria into alumina resulted in a decrease in ceria particle size but did not significantly affect the size of alumina particles. However, the introduction of ceria into alumina led to an increase in the BET surface area of mixed oxides in contrast with that for pure alumina. Deposition of gold using urea and thoroughly washing of freshly prepared catalysts with ammonia solution perhaps also played an important role, providing a fine dispersion of gold species on the defect-rich surface of nanostructured oxides. Transient analysis of CO oxidation results in estimation of the relative content of (Au–ceria vacancy) active sites in catalysts. These data are in good agreement with the order of activity for tested samples and gold dispersion values previously obtained with EXAFS data.

Thus, the gold catalysts based on nanostructured ceria–alumina mixed oxides prepared by sol–gel are characterized by high content of active sites including gold species and ceria vacancies. The following factors: preparation procedure of nanostructured mixed oxides by sol–gel, deposition–precipitation of gold precursor with urea and washing of freshly prepared gold catalysts with ammonia solution play an important role in the formation of gold species with high catalytic activity in CO oxidation.

Acknowledgments

The authors thank E. Flores, P. Casillas, V. Garcia, M. Sainz, F. Ruiz, G. Vilchis, E. Aparicio, J. Peralta, J. Palomares, and M. Vega for technical support. M.I. Perez Montfort corrected the English version of the manuscript. This research project was supported by DGAPA-PAPIIT (UNAM, México) through Grant IN 224510. The authors also wish to acknowledge the Environmental Nanotechnology University Program (PUNTA-UNAM) and CONACYT grant 50547 for their support.

References

[1] M. Haruta, N. Yamada, T. Kobayashi, S. Iijima, J. Catal. 115 (1989) 301–309.
[2] G.C. Bond, D.T. Thompson, Catal. Rev. Sci. Eng. 41 (1999) 19–388.
[3] D. Andreeva, V. Idakiev, T. Tabakova, A. Andreev, R. Giovanoli, Appl. Catal. A: Gen. 134 (1996) 275–283.
[4] F. Boccuzzi, A. Chiorino, M. Manzoli, D. Andreeva, T. Tabakova, J. Catal. 188 (1999) 176–185.
[5] D. Andreeva, V. Idakiev, T. Tabakova, A. Andreev, J. Catal. 158 (1996) 354–355.
[6] S. Tsubota, T. Nakamura, K. Tanaka, M. Haruta, Catal. Lett. 56 (1998) 131–135.
[7] M. Haruta, S. Tsubota, T. Kobayashi, H. Kageyama, M.J. Genet, B. Delmon, J. Catal. 144 (1993) 175–192.
[8] D.A.H. Cunningham, W. Vogel, H. Kageyama, S. Tsubota, M. Haruta, J. Catal. 177 (1998) 1–10.
[9] S. Carrettin, P. Concepción, A. Corma, J.M.L. Nieto, V.F. Puntes, Angew. Chem. Int. Ed. 43 (2004) 2538–2540.
[10] J. Guzman, S. Carrettin, A. Corma, JACS 127 (2005) 3286–3287.
[11] U.R. Pillai, S. Deevi, Appl. Catal. A: Gen. 299 (2006) 266–273.
[12] Q. Fu, S. Kudriavtseva, H. Saltsburg, M. Flytzani-Stephanopoulos, J. Chem. Eng. 93 (2003) 41–53.
[13] Q. Fu, H. Saltsburg, M. Flytzani-Stephanopoulos, Science 301 (2003) 935–938.
[14] X. Wang, J.A. Rodriguez, J.C. Hanson, M. Perez, J. Evans, J. Chem. Phys. 123 (2005) 221101–221105.
[15] M.A. Centeno, K. Hadjiivanov, Tz. Venkov, Hr. Klimev, J.A. Odriozola, J. Mol. Catal. A: Chem. 252 (2006) 142–149.
[16] L. Ilieva, G. Pantaleo, I. Ivanov, A.M. Venezia, D. Andreeva, Appl. Catal. B: Environ. 65 (2006) 101–109.
[17] R. Ramirez-Lopez, L. Balderas-Tapia, I. Elizalde-Martinez, T. Viveros, Chem. Eng. Comm. 196 (2009) 1189–1197.
[18] A. Martinez-Arias, M. Fernández-Garcia, L.N. Salamanaca, R.X. Valenzuela, J.C. Conesa, J. Soria, J. Phys. Chem. B 104 (2000) 4038–4046.
[19] D. Andreeva, I. Ivanov, L. Ilieva, J.W. Sobczak, G. Avdeev, T. Tabakova, Appl. Catal. A: Gen. 333 (2007) 153–160.
[20] G. Perez, S. Fuentes, V. Petranovskii, A. Simakov, Catal. Lett. 110 (2006) 53–60.
[21] G. Perez, F. Castillon, A. Simakov, H. Tiznado, F. Zaera, S. Fuentes, Appl. Catal. B: Environ. 69 (2007) 219–225.
[22] J.B. Miller, E.I. Ko, Catal. Today 35 (1997) 269–292.
[23] A. Vazquez, T. Lopez, R. Gomez, X. Bokhimi, J. Mol. Catal. 167 (2001) 91–99.
[24] R. Zanella, S. Giorgio, C.R. Henry, C. Louis, J. Phys. Chem. B 106 (2002) 7634–7642.
[25] R. Zanella, L. Delannoy, C. Louis, Appl. Catal. A: Gen. 291 (2005) 62–72.
[26] A.P. Ferreira, D. Zanchet, R. Rinald, U. Schuchardt, S. Damyanova, J.M.C. Buenoa, Appl. Catal. A: Gen. 388 (2010) 45–56.
[27] M.A. Centeno, C. Portales, I. Carrizosa, J.A. Odriozola, Catal. Lett. 102 (2005) 289–297.
[28] G. Ranga Rao, H. Ranjan Sahu, Proc. Indian Acad. Sci. (Chem. Sci.) 113 (2001) 651–658.
[29] A. Escobedo Morales, E. Sanchez Mora, U. Pal, Revista Mexicana de Fisica S 53 (2007) 18–22.
[30] A. Corma, P. Atienzar, H. Garcia, J.-Y. Chane-Ching, Nature Mater. 3 (2004) 394–397.
[31] T. Masui, K. Fujiwara, K. Machida, G. Adachi, Chem. Mater. 9 (1997) 2197–2204.
[32] Y.-W. Zhang, R. Si, Ch.-Sh. Liao, Ch.-H. Yan, J. Phys. Chem. B 107 (2003) 10159–10167.
[33] S. Ivanova, C. Petit, V. Pitchon, Appl. Catal. A: Gen. 267 (2004) 191–201.
[34] http://en.wikipedia.org/wiki/Isoelectric_point.
[35] D. Andreeva, V. Idakiev, T. Tabakova, L. Ilieva, P. Falaras, A. Bourlinos, A. Travlos, Catal. Today 72 (2002) 51–57.
[36] T. Akita, M. Okumura, K. Tanaka, M. Kohyama, M. Haruta, Catal. Today 117 (2006) 62–68.
[37] J.F. Moulder, W.F. Stickle, P.E. Sobol, K.D. Bomben, Handbook of X-ray Photoelectron Spectroscopy, Perkin-Elment/Corporation Physical Electronics Division, Eden Prairie, 1992, p. 179.
[38] A.M. Visco, F. Neri, G. Neri, A. Donato, C. Milone, S. Galvagno, Phys. Chem. Chem. Phys. 1 (1999) 2869–2873.
[39] F.-W. Chang, H.-Y. Yu, L.S. Roselin, H.-C. Yang, T.-C. Ou, Appl. Catal. A: Gen. 302 (2006) 157–167.
[40] V.V. Kriventsov, I.L. Simakova, A. Simakov, E. Smolentseva, F. Castillon, M. Estrada, E. Vargas, D.P. Ivanov, B.N. Novgorodov, D.I. Kochubey, S. Fuentes, Nucl. Instr. Method Phys. Res. A 603 (2009) 185–187.

[41] A.V. Simakov, V.V. Kriventsov, I.L. Simakova, E. Smolentseva, F. Castillon, M. Estrada, E. Vargas, E.P. Yakimchuk, D.P. Ivanov, D.G.Aksenov, D.V. Andreev, B.N. Novgorodov, D.I. Kochubey, S. Fuentes, Surf. Invest. J. X-ray Synchrotron Neutron Tech. 4 (2010) 630–635.
[42] S. Ivanova, V. Pitchon, Y. Zimmermann, C. Petit, Appl. Catal. A: Gen. 298 (2006) 57–64.
[43] A. Corma, H. Garcia, Chem. Soc. Rev. 37 (2008) 2096–2126.
[44] O.V. Komova, A.V. Simakov, G.A. Kovalenko, N.A. Rudina, T.V. Chuenko, N.A. Kulikovskaya, J. Kinet. Catal. 48 (2007) 803–811.
[45] Q. Fu, W. Deng, H. Saltsburg, M. Flytzani-Stephanopoulos, Appl. Catal. B: Environ. 56 (2005) 57–68.
[46] B. Campo, M. Volpe, S. Ivanova, R. Touroude, J. Catal. 242 (2006) 162–171.
[47] Y. Azizi, C. Petit, V. Pitchon, J. Catal. 256 (2008) 338–344.
[48] T. Salama, T. Shido, R. Ohnishi, M.J. Ichikawa, J. Phys Chem. 100 (1996) 3688–3694.
[49] V.W.-W. Yam, C.-L. Chan, C.-K. Li, K.M.-C. Wong, Coord. Chem. Rev. 216-217 (2001) 173–194.
[50] E. Smolentseva, A. Pestryakov, N. Bogdanchikova, A. Simakov, M. Avalos, M. Farias, J.A. Diaz, V. Gurin, A. Tompos, Int. J. Mod. Phys. 19 (2005) 2496–2501.
[51] W. Chen, J. Zhang, W. Cai, Scr. Mater. 48 (2003) 1061–1066.
[52] I. Tuzovskaya, N. Bogdanchikova, A. Simakov, V. Gurin, A. Pestryakov, M. Avalos, M. Farias, Chem. Phys. 338 (2007) 23–32.
[53] G. Avgouroulos, M. Manzoli, F. Boccuzzi, T. Tabakova, J. Papavasiliou, T. Ioannides, V. Idakiev, J. Catal. 256 (2008) 237–247.
[54] M. Manzoli, F. Vindigni, A. Chiorino, T. Tabakova, V. Idakiev, F. Boccuzzi, React. Kinet. Catal. Lett. 91 (2007) 213–221.
[55] M. Manzoli, F. Boccuzzi, A. Chiorino, F. Vindigni, W. Deng, M. Flytzani-Stephanopoulos, J. Catal. 245 (2007) 308–315.
[56] F. Menegazzo, F. Pinna, M. Signoretto, V. Trevisan, F. Boccuzzi, A. Chiorino, M. Manzoli, Appl. Catal. A: Gen. 356 (2009) 31–35.
[57] V. Aguilar-Guerrero, B.C. Gates, J. Catal. 260 (2008) 351–357.
[58] Y. Guan, M. Ligthart, G.D. Elzinga, J.-P.A.Z. Pieterse, R.A. van Santen, E.J.M. Hensen, unpublished results.
[59] S.-Y. Lai, Y. Qiu, S. Wang, J. Catal. 237 (2006) 303–313.
[60] A.M. Venezia, G. Pantaleo, A. Longo, G. Di Carlo, M. Casaletto, F.L. Liotta, G. Deganello, J. Phys. Chem. B 109 (2005) 2821–2827.
[61] S.A.C. Carabineiro, S.S.T. Bastos, J.J.M. Órfão, M.F.R. Pereira, J.J. Delgado, J.L. Figueiredo, Appl. Catal. A: Gen. 381 (2010) 150–160.
[62] J.T. Miller, A.J. Kropf, Y. Zha, J.R. Regalbuto, L. Delannoy, C. Louis, E. Bus, J.A. van Bokhoven, J. Catal. 240 (2006) 222–234.
[63] S.L. Shannon, J.G. Goodwin, Appl. Catal. A: Gen. 151 (1997) 3–26.
[64] R.J. Berger, F. Kapteijn, J.A. Moulijn, G.B. Marin, J. De Wilde, M. Olea, D. Chen, A. Holmen, L. Lietti, E. Tronconi, Y. Schuurman, Appl. Catal. A: Gen. 342 (2008) 3–28.
[65] Z. Song, W. Liu, H. Nishiguchia, Catal. Commun. 8 (2007) 725–730.
[66] E.V. Kondratenko, Y. Sakamoto, K. Okumura, H. Shinjoh, Catal. Today 164 (2011) 46–51.